

Design of low bandgap tin–lead halide perovskite solar cells to achieve thermal, atmospheric and operational stability

Rohit Prasanna^{1,2}, Tomas Leijtens^{1,2,3}, Sean P. Dunfield^{2,4}, James A. Raiford⁵, Eli J. Wolf^{1,2}, Simon A. Swifter¹, Jérémie Werner^{2,6}, Giles E. Eperon², Camila de Paula⁵, Axel F. Palmstrom², Caleb C. Boyd^{1,2}, Maikel F. A. M. van Hest², Stacey F. Bent⁵, Glenn Teeter², Joseph J. Berry² and Michael D. McGehee^{2,4,6*}

Low bandgap tin–lead iodide perovskites are key components of all-perovskite tandem solar cells, but can be unstable because tin is prone to oxidation. Here, to avoid a reaction with the most popular hole contact, we eliminated polyethylenedioxythiophene:polystyrenesulfonate as a hole transport layer and instead used an upward band offset at an indium tin oxide–perovskite heterojunction to extract holes. To suppress oxidative degradation, we improved the morphology to create a compact and large-grained film. The tin content was kept at or below 50% and the device capped with a sputtered indium zinc oxide electrode. These advances resulted in a substantially improved thermal and environmental stability in a low bandgap perovskite solar cell without compromising the efficiency. The solar cells retained 95% of their initial efficiency after 1,000 h at 85 °C in air in the dark with no encapsulation and in a damp heat test (85 °C with 85% relative humidity) with encapsulation. The full initial efficiency was maintained under operation near the maximum power point and near 1 sun illumination for over 1,000 h.

Recent breakthroughs in the fabrication of ABX₃ perovskites in which B is a mixture of tin and lead and the bandgaps are <1.3 eV have enabled the construction of all-perovskite tandem solar cells that promise to exceed the efficiencies that single-junction solar cells are limited to^{1,2}, while keeping the benefits of low-cost and low-temperature fabrication for both subcells^{3–9}. Tin at the B site has been crucial to achieving the low bandgaps required in the rear cell absorber of a tandem^{10,11}. However, tin-containing perovskites face unique stability challenges because tin can be oxidized from the 2+ to the 4+ state. A small amount of oxidized tin in the perovskite has been theorized to cause fast recombination, which results in short carrier diffusion lengths^{12,13}. Further oxidation can lead to a complete breakdown of the perovskite absorber and a drastic reduction in photocurrent.

Solar cells based on perovskites with only lead at the B site maintain their performance when aged under environmental stressors, which include exposure to elevated temperature (85 °C for 1,000 h), damp heat (85 °C with 85% relative humidity) and operation at the maximum power point under continuous illumination^{14–19}. So far, however, nothing close to these demonstrations of stability has been achieved for tin-containing perovskites. Early perovskite solar cells with pure tin at the B site exhibited complete degradation of performance within minutes of exposure to air¹². More recent reports of FA_{1–x}Cs_xSnI₃ and CsSnI₃ solar cells show a more than 30% drop in performance within a few hours of exposure to air^{20,21}.

Recent studies demonstrated that alloyed tin–lead perovskite films show a stabilization towards oxidation compared with pure tin perovskites²²—which is fortuitous given that the mixed tin–lead perovskites also have close-to-ideal bandgaps for tandem solar

cells. However, good stability has yet to be realized in full devices. Some recent studies investigated the stability of tin–lead perovskite solar cells, but performed stability tests only in an inert atmosphere and/or at room temperature, and they often showed degradation within relatively short times of less than 100 h (refs. ^{23–25}). One report showed an improved stability using a coherent two-dimensional–three-dimensional (2D–3D) tin–lead perovskite, but it still showed performance drops of over 30% after 1,000 h of illumination in nitrogen²⁶.

Here we designed the composition, film morphology and device architecture of a tin–lead iodide perovskite solar cell to enable stable operation. We found that the commonly used hole transporter polyethylenedioxythiophene:polystyrenesulfonate (PEDOT:PSS) reacts adversely with tin–lead perovskites, which leads to severely worsened charge extraction after thermal ageing. We fabricated a solar cell using an indium tin oxide (ITO)–perovskite heterojunction without a dedicated hole transport layer to achieve thermal stability with little or no loss in efficiency over the 1,000 h period examined. The increasing compactness and grain size of the tin–lead perovskite films suppressed the oxidative degradation at morphological domain boundaries. Using a FA_{0.75}Cs_{0.25}Sn_{0.4}Pb_{0.6}I₃ perovskite (bandgap of 1.29 eV) film with increased grain compactness and size (350 nm on average) in a solar cell with no hole transport layer and a sputtered indium zinc oxide (IZO) capping electrode, we demonstrated the retention of 100% of the initial efficiency on ageing for 1,000 h at 85 °C in air without encapsulation. With glass-on-glass encapsulation, the device maintained 95% of its initial efficiency under damp heat ageing for 1,000 h at 85 °C with 85% relative humidity (conditions specified in the IEC 61646

¹Materials Science and Engineering, Stanford University, Stanford, CA, USA. ²National Renewable Energy Laboratory, Golden, CO, USA. ³Swift Solar, San Carlos, CA, USA. ⁴Materials Science and Engineering Program, University of Colorado, Boulder, CO, USA. ⁵Chemical Engineering, Stanford University, Stanford, CA, USA. ⁶Chemical and Biological Engineering, University of Colorado, Boulder, CO, USA. *e-mail: michael.mcgehee@colorado.edu

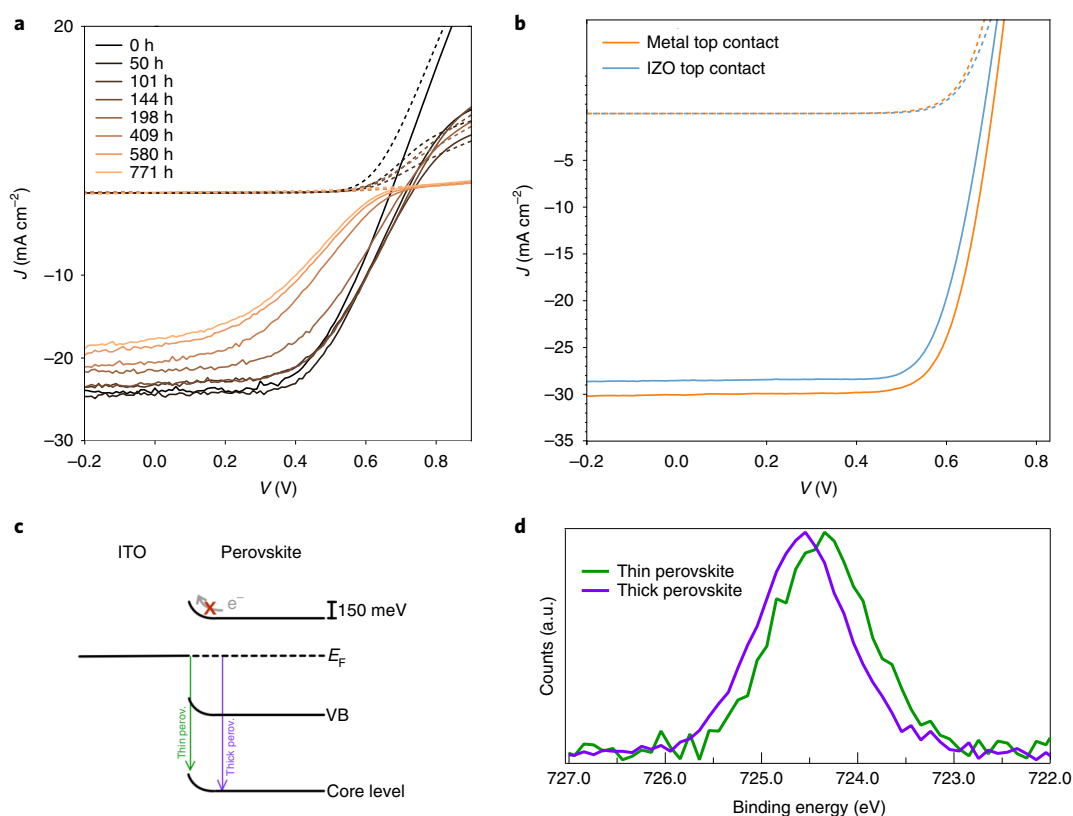


Fig. 1 | Replacement of PEDOT:PSS with an ITO-perovskite heterojunction as the hole contact. **a**, J - V curves of a large-grained $\text{FA}_{0.75}\text{Cs}_{0.25}\text{Sn}_{0.4}\text{Pb}_{0.6}\text{I}_3$ solar cell, with PEDOT:PSS as the hole transport layer as a function of ageing time at 85 °C in air. **b**, J - V curves of a $\text{FA}_{0.75}\text{Cs}_{0.25}\text{Sn}_{0.4}\text{Pb}_{0.6}\text{I}_3$ solar cell fabricated on ITO without a hole transport layer, capped with either silver (opaque) or sputtered IZO (semitransparent). Device stack: ITO/ $\text{FA}_{0.75}\text{Cs}_{0.25}\text{Sn}_{0.4}\text{Pb}_{0.6}\text{I}_3$ perovskite/ C_{60} /BCP-Ag or SnO_2 -IZO. Light J - V curves shown as solid lines and dark J - V curves as dashed lines. **c**, Band offsets at the ITO- $\text{FA}_{0.75}\text{Cs}_{0.25}\text{Sn}_{0.4}\text{Pb}_{0.6}\text{I}_3$ perovskite heterojunction that leads to the extraction of holes but the blocking of electrons, measured by XPS. Binding energies of a generic perovskite core level are depicted schematically for a thin (green) and thick (purple) perovskite. E_F , Fermi level; VB, valence band edge. **d**, Positions of the Cs 3d XPS peak in a thin (4 nm) and a thick (450 nm) layer of perovskite on ITO. a.u., arbitrary units.

standard)²⁷. Finally, we demonstrated a stable operation at a 15.4% power conversion efficiency (PCE) under continuous illumination in nitrogen for 1,000 h.

ITO-perovskite junction as thermally stable hole contact

We recently reported that alloying tin with lead drastically retards the oxidation of tin-containing perovskites by forcing the reaction to adopt a less favourable pathway that involves breaking more Sn-I bonds²². Using a lower tin content to improve the stability raises the bandgap to a larger-than-ideal value. However, modelling showed that practical tandems, not ones at the theoretical limit, with a rear cell having 40% tin can still reach an efficiency of 31%, only 1 percentage point lower than that achievable with a less stable tin content of 60% (ref. ²). For this study, therefore, we chose the composition $\text{FA}_{0.75}\text{Cs}_{0.25}\text{Sn}_{0.4}\text{Pb}_{0.6}\text{I}_3$ (FA, formamidinium). We used FA and caesium at the A site, which have been shown to achieve better thermal stability than the more volatile methylammonium^{14,28–30} and also, for tin-lead perovskites, better stability under light⁶.

The majority of efficient tin-lead perovskite solar cells reported to date use PEDOT:PSS as the hole transport layer. However, on ageing for 100–300 h at 85 °C, the tin-lead perovskite solar cells on PEDOT:PSS developed an S-kink in the current–voltage (J - V) curve, suggesting diminishing carrier extraction, which is often induced by insulating layers or energy level mismatches (Fig. 1a and Leijtens et al.⁶). This degradation occurred similarly when the cell was aged in an inert atmosphere (Supplementary Fig. 1) and occurred for devices based on both small-grained and large-grained

perovskites. As a control, we aged substrates with just PEDOT:PSS on ITO at the same temperature (85 °C) and then fabricated the rest of the solar cell; these devices performed similarly to devices fabricated on freshly deposited PEDOT:PSS and showed no S-kink—this indicates that the problem is not one of PEDOT:PSS reacting with or etching the ITO substrate, or of any degradation within the PEDOT:PSS layer alone. Furthermore, pure-lead perovskite solar cells with PEDOT:PSS have been shown to be thermally stable, with no S-kinks forming under ageing at elevated temperatures³¹. We conclude that the interface between PEDOT:PSS and tin-lead perovskites shows poor thermal stability, with increasingly poor charge extraction under ageing at elevated temperatures.

To solve this problem, we fabricated hole-transport-layer-free solar cells without a hole transport layer, with the perovskite deposited directly on the ITO and the common electron transport bilayer of C_{60} and bathocuproine (BCP) over the perovskite. Figure 1b shows that the device with the perovskite directly on the ITO, with no dedicated hole transport layer, showed a good solar cell performance, as it attained a stabilized PCE of 15.4% (as measured from continuous maximum power point tracking). The voltage was 0.70 V despite the lack of a selective contact and a high short-circuit current (J_{SC}) of 30.2 mA was harvested, which matched that measured from integrating the external quantum efficiency spectrum (Supplementary Fig. 2). Using a perovskite composition ($\text{FA}_{0.75}\text{Cs}_{0.25}\text{Sn}_{0.5}\text{Pb}_{0.5}\text{I}_3$) and the device structure reported in highly efficient all-perovskite tandem solar cells⁶, we achieved a mere 0.2% absolute drop in performance compared to a less stable architecture

that uses PEDOT:PSS (as shown in Supplementary Fig. 3, the PEDOT-based device reached a 16.6% efficiency, whereas the device on bare ITO achieved an efficiency of 16.4%) and achieved the same open circuit voltage (V_{OC}) of 0.72 V. The architecture we developed, without a dedicated hole transport layer, can easily be translated into monolithic all-perovskite tandem solar cells—we fabricated efficient tandems in this architecture that exceeded the efficiency of the less stable PEDOT-containing tandems fabricated side by side in the same batch, and reached close to 21% efficiency (Supplementary Fig. 4).

To investigate the band structure of the ITO–perovskite heterojunction and why it is favourable for hole extraction, we used X-ray photoelectron spectroscopy (XPS) to directly measure band offsets in the perovskite near the ITO interface with a previously demonstrated method³². The core level binding energy in XPS is measured with reference to the Fermi level. As the Fermi level must be flat across the heterojunction at equilibrium, band bending or band offset near an interface produces a shift of the core level XPS peaks of perovskite at the interface compared with those in the bulk (Fig. 1c). We fabricated a very thin (4 nm) layer of perovskite on ITO to probe the band positions near the interface and a separate film of 450 nm thick perovskite on ITO to probe those far from the interface (fabrication details are given in Methods); further, we verified that relative XPS core level peak heights were close to those expected for the correct perovskite composition. As Fig. 1d shows, the Cs 3d level shifted to a higher binding energy by 150 meV on going from interface to bulk perovskite. The valence band edge and other core levels in the perovskite showed a similar shift (Supplementary Figs. 6 and 7), which indicates that the perovskite bands shifted upward by 150 meV near the interface with ITO. We verified that all XPS peaks remained unchanged throughout the measurement (Supplementary Fig. 8), which confirms that there was no effect of any beam damage in either the thin or thick sample. The resulting band diagram of the ITO–perovskite junction (Fig. 1c) rationalizes how devices without a dedicated hole transport layer are capable of generating a substantial (V_{OC}): an upward band shift in the perovskite at the junction with ITO results in electrons being blocked but hole extraction being facilitated. This upward band shift probably helps prevent electrons from recombining with holes in the ITO. In addition to energetic alignment, it is possible that factors related to the chemistry of the interface between ITO and tin–lead perovskite might help to suppress recombination there, which future work could study.

The formation of this Schottky-type junction with an upward band offset in the perovskite probably works with tin–lead perovskites because they have energy levels that are shallower by 300–500 meV than those of pure lead perovskites¹¹, and specifically a Fermi level that is shallower than that of ITO. Pure lead perovskites showed poor performance in solar cells fabricated without a dedicated hole selective layer (Supplementary Fig. 9)—they have energy levels that are significantly deeper (by 300–500 meV) than those of the low bandgap tin–lead perovskites. This probably implies the absence of the upward band offset that is present in tin–lead devices of this architecture, which helps block electrons from reaching the ITO interface and recombining with holes there.

For stability tests at 85 °C, instead of using a BCP–silver top contact, we used a bilayer of tin oxide and zinc-doped tin oxide to serve as an electron-selective sputter buffer and capped the device with 200 nm of sputtered IZO. This stack has been shown to protect the perovskite from decomposition due to volatilization of the organic cations on ageing at elevated temperatures³¹. We did not use a metal top contact, because diffusion of metal into the perovskite has been shown to be an extrinsic source of degradation in perovskite solar cells at elevated temperatures. The lack of a reflective metal electrode results in a lower J_{SC} . Although work from our group has shown ways to improve the barrier properties of a sputtered metal oxide so that it successfully prevents metal diffusion³³, for tests at

elevated temperatures in the present study, we refrained from using a metal contact to focus on proving the intrinsic thermal and atmospheric stability of the tin–lead perovskite device. It is important for future work to find ways to deposit an impermeable electrode on tin–lead perovskite solar cells to maintain stability with the metal contacts.

Improved morphology to suppress oxidation

We investigated the effect of perovskite morphology on stability at 85 °C in air. We prepared devices of the same perovskite composition ($FA_{0.75}Cs_{0.25}Sn_{0.4}Pb_{0.6}I_3$) but of differing compactness and size of morphological domains (details in Methods)³⁴. For simplicity, we refer to these hereafter as small- and large-grained films, but we note that the ‘grains’ visible in scanning electron microscopy (SEM) images of perovskite films are probably not single crystals but morphological domains—high-resolution transmission electron microscopy has shown actual single crystalline domains much smaller (around tens of nanometres) than the grains typically observed in SEM, and mapping studies have observed twin boundaries within such grains^{35,36}.

Figure 2a,b shows the evolution of the J – V curve of small- and large-grained $FA_{0.75}Cs_{0.25}Sn_{0.4}Pb_{0.6}I_3$ solar cells, respectively (both without a dedicated hole transport layer) with time in air at 85 °C. The small-grained device, in addition to showing a poorer initial performance, deteriorated on ageing at 85 °C in air to form an S-kink and lose current within 100 h of ageing. The S-kink and current loss did not occur on ageing a similar small-grained device in nitrogen at 85 °C (Supplementary Fig. 10), which suggests they are related to oxygen-induced degradation.

To probe the spatial location of the oxidation of tin–lead perovskite, we heated a bare film of large-grained $FA_{0.75}Cs_{0.25}Sn_{0.4}Pb_{0.6}I_3$ to 120 °C in air for 20 minutes and measured an elemental depth profile by XPS, sputtering with argon ions between successive XPS acquisitions to generate the depth profile (Fig. 2f). The top-surface XPS spectrum (before any sputtering) shows a clear oxygen peak. Integrating the XPS peak intensities show that, in addition to tin in the perovskite, the surface has tin and oxygen in a 1:2 ratio, consistent with the formation of tin oxide (SnO_2) by partial oxidation of the perovskite. XPS spectra at increasing depths show diminishing amounts of oxygen, until several spectra deep inside the film show no oxygen peak at all (Fig. 2). This profile shows that the oxidation of the perovskite begins at exposed surfaces.

We proceeded to measure the d.c. conductance of the perovskite after increasing amounts of oxidation to elucidate the mechanism of the drop in performance of the small-grained films. The formation of Sn^{4+} due to oxidation should increase the conductivity, whereas the formation of tin oxide at grain surfaces should result in a drop in the long-range conductance because it is relatively insulating. We measured the d.c. conductance by applying a bias and measuring the current across lateral gold electrodes (4 mm long) evaporated onto the perovskite (Supplementary Fig. 11). We used varying channel lengths to verify that the measured conductance was dominated by the perovskite rather than any effects of contact resistance (Supplementary Fig. 12). Furthermore, the J – V curve of the lateral electrode device was linear and symmetric (Supplementary Fig. 13), which confirmed that contact was Ohmic and the measurement was not significantly affected by any potential barriers created by mobile ionic species in the perovskite.

Figure 3a shows the d.c. conductance of films of either small- or large-grained $FA_{0.75}Cs_{0.25}Sn_{0.4}Pb_{0.6}I_3$ films on glass as a function of time spent at 85 °C in air. Within the first four minutes of ageing, the conductance increased by over four orders of magnitude. We ascribe this large increase in conductance to the formation of tin vacancies and compensating holes, which several studies have shown to form on the oxidation of tin-containing perovskites¹³. At longer ageing times, the conductance dropped. Interestingly, the conductance of the small-grained film decreased faster and

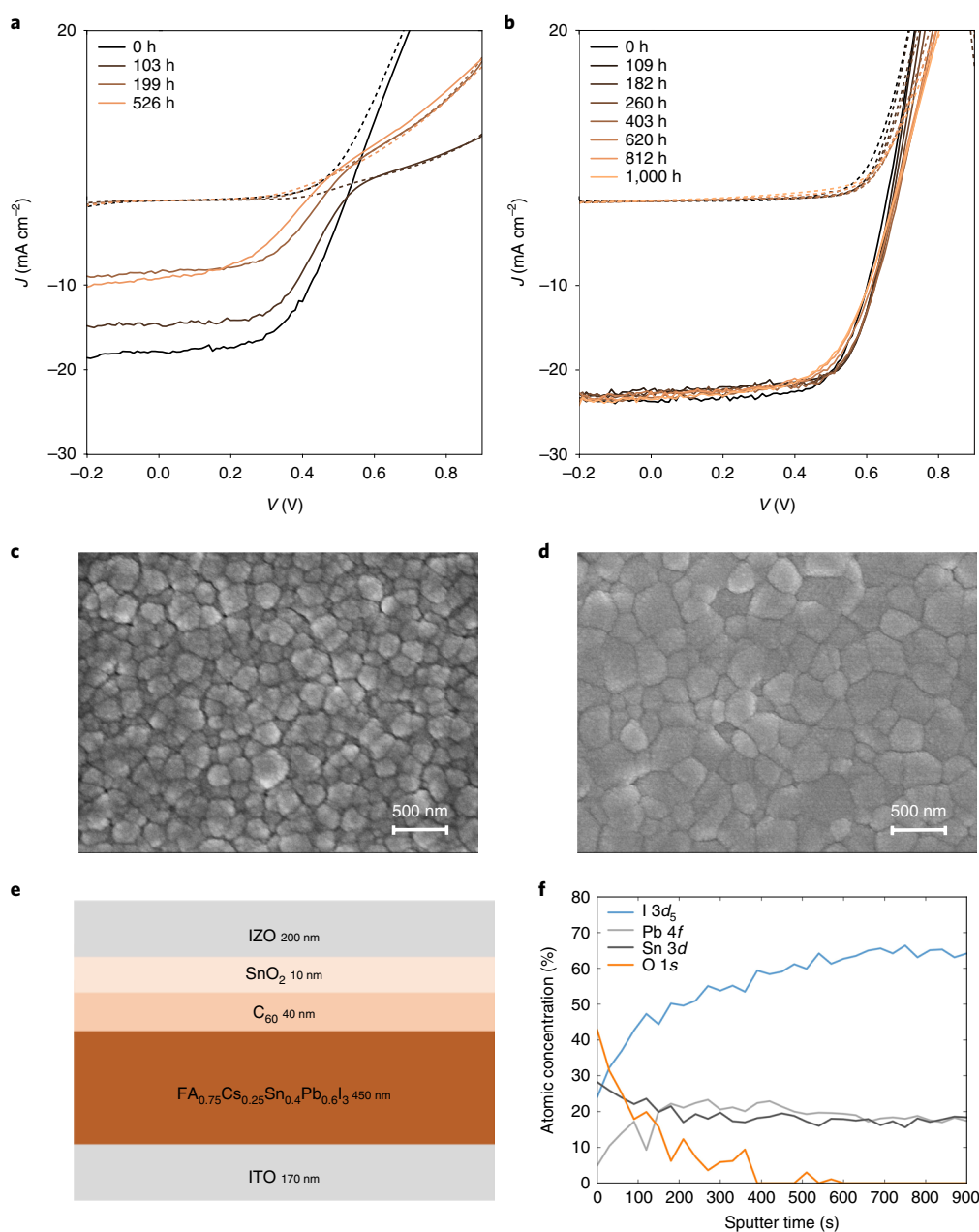


Fig. 2 | Thermal and atmospheric stability of tin-lead perovskite solar cells. a,b, J - V curves of small-grained (**a**) and large-grained (**b**) devices as a function of ageing time at 85 °C in air. Light J - V curves are shown as solid lines and dark J - V curves as dashed lines. J_{sc} values here are lower than the true 1 sun J_{sc} due to the use of a lower intensity lamp for testing devices under thermal ageing—however, the same lamp was used to test both small- and large-grained devices. **c,d**, SEM top-view images of small-grained (**c**) and large-grained (**d**) perovskite solar cells. **e**, Schematic of the device stack used for the solar cells for thermal stability testing. **f**, Atomic concentrations as a function of depth from the top surface of a bare large-grained $\text{FA}_{0.75}\text{Cs}_{0.25}\text{Sn}_{0.4}\text{Pb}_{0.6}\text{I}_3$ film that has been partially oxidized by heating at 120 °C in air for 20 min, measured by XPS depth profiling.

by far more than that of the large-grained film, despite both having the same perovskite composition—in 28 minutes of air ageing, the small-grained film dropped by a factor of a 100 from its peak, whereas the large-grained film dropped by less than a factor of 5 (Supplementary Note 1).

Comparing the initial conductances of the small- and large-grained films gives insight into the difference in their rates of oxidation. The initial conductance of the small-grained film was $1.1 \times 10^{-7} \text{ S cm}^{-1}$, an order of magnitude lower than that of the large-grained film, $1.46 \times 10^{-6} \text{ S cm}^{-1}$. These values are two and three orders of magnitude higher, respectively, than the reported

conductance of MAPbI_3 (MA, methylammonium)³⁷, which is consistent with literature reports that there is a higher background carrier density in tin-containing perovskites^{13,38}. SEM images showed an increased compactness and less space between the morphological domains for the large-grained film (Fig. 2c,d). We expect that the lower conductance for the small-grained film is due to the more frequent and wider domain boundaries, which leads to a lower long-range mobility. The morphology also explains the faster oxidation in the small-grained film. As the XPS depth profile in Fig. 2f shows, oxidation begins at the exposed surfaces. Wider and more frequent domain boundaries, therefore, lead to a faster oxidation

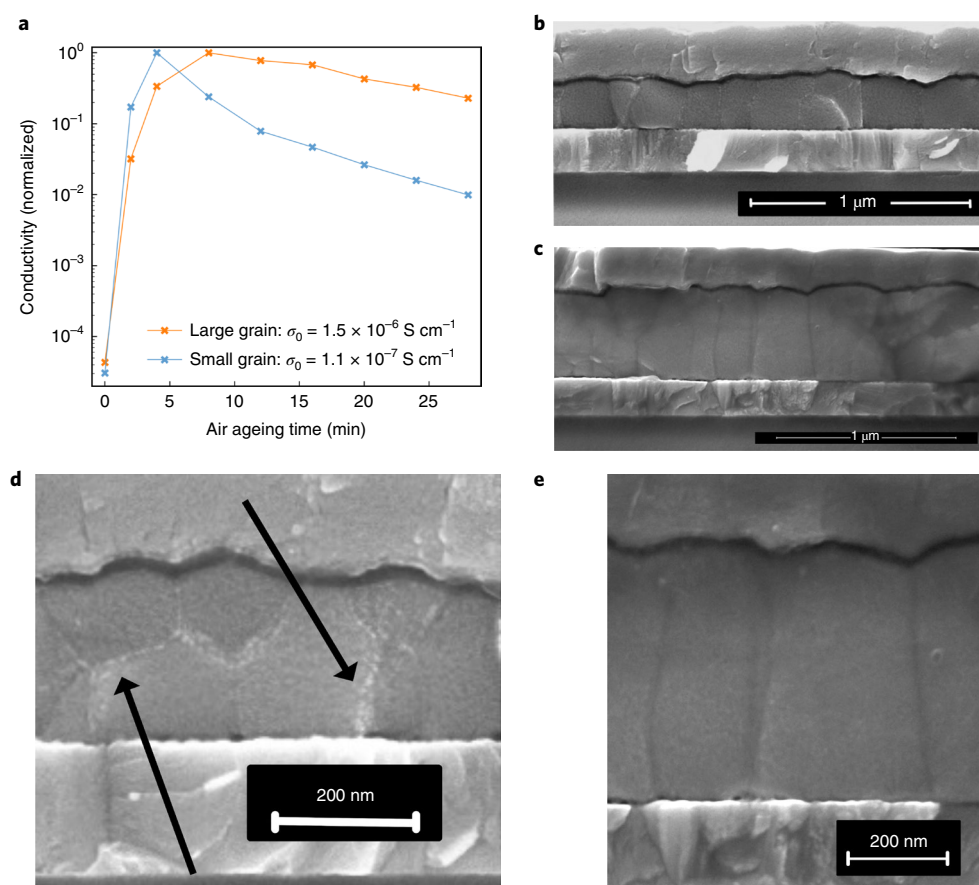


Fig. 3 | Morphology dependence of tin-lead perovskite oxidation. **a**, d.c. conductance of two perovskite films of the same composition ($\text{FA}_{0.75}\text{Cs}_{0.25}\text{Sn}_{0.4}\text{Pb}_{0.6}\text{I}_3$) but different grain compactness and size as a function of time spent at 85 °C in air. The conductance values are normalized to their maximum value for each film and the initial values of the conductance are denoted as σ_0 in the legend. Lines are a guide to the eye. **b,c**, Cross-sectional SEM images of small-grained (**b**) and large-grained (**c**) devices (both on bare ITO without a hole transport layer) after ageing in air at 85 °C for 500 h. **d,e**, Magnified views of the cross-section of small-grained (**d**) and large-grained (**e**) devices after air ageing. The arrows highlight the bright edges observed at grain boundaries after air ageing in the small-grained device.

and larger amounts of insulating tin oxide being formed, which lead to larger drops in the conductance. High-resolution cross-sectional SEM images of devices aged at 85 °C in air for 500 h (Fig. 3) showed bright regions at the domain boundaries in only the small-grained device, which is consistent with oxidation at these boundaries having caused degradation of the device performance and the d.c. conductance of the small-grained devices and films.

Thermal, atmospheric and operational stability

Solar cells made from the large-grained, thick perovskite film displayed an impressive stability—specifically, there is no noticeable loss in J_{SC} or V_{OC} (Fig. 4a), which indicates that the perovskite in the device remained stable to oxidation under ageing in air at elevated temperatures without any additional encapsulation beyond the protection provided by the capping IZO electrode. The stability was reproducible across the eight devices tested—on average, the solar cells maintained 95% of their starting efficiency after ageing at 85 °C in air for 1,000 h.

We proceeded to use an encapsulation technique we recently applied to lead-based perovskite solar cells to test the damp heat stability at 85 °C with 85% relative humidity¹⁷. Briefly, the package uses glass-on-glass encapsulation with a low-elastic-modulus (7 MPa) polyolefin encapsulant and a butyl rubber edge seal, with on-substrate conductive feedthroughs to make contact to the solar cell (Supplementary Fig. 14). Packaged $\text{FA}_{0.75}\text{Cs}_{0.25}\text{Sn}_{0.4}\text{Pb}_{0.6}\text{I}_3$ solar cells with the hole-transporting material (HTM)-free device stack

described above maintained 95% of their initial efficiency on ageing for 1,000 h at 85 °C and 85% relative humidity (Fig. 4a).

Finally, we probed device stability under constant illumination by a sulfur plasma lamp at 0.8 sun with cells kept close to the maximum power point in nitrogen. There was an initial light-soak period during which the cells showed an improvement in V_{OC} . For cells with C_{60} , BCP, and silver as the top contact, a slow drop in photocurrent appeared, starting at around 900 h, which we ascribe to the effects of metal diffusion into the perovskite as we and others have shown for pure lead perovskites^{33,39}. For cells in the architecture ITO/ $\text{FA}_{0.75}\text{Cs}_{0.25}\text{Sn}_{0.4}\text{Pb}_{0.6}\text{I}_3$ (compact, large-grained)/ C_{60} /SnO₂/ITO with no metal top contact, devices remained above 100% of the starting efficiency for the full 1,000 h (Fig. 4b).

Conclusions

This study implemented a series of advances (to alloy tin with lead for a drastic improvement in oxidation stability, to avoid adverse reactions at the hole contact–perovskite interface and to improve the perovskite morphology) to demonstrate the stability of full solar cells based on a low bandgap tin–lead perovskite. The use of an ITO–perovskite heterojunction as the hole contact instead of acidic PEDOT:PSS enabled the maintenance of over 95% of the initial performance over 1,000 h of ageing at 85 °C. An improved compact morphology, together with keeping the tin content at 50% or below and using a capping transparent conducting oxide electrode, enabled the maintenance of performance over 1,000 h at 85 °C in air

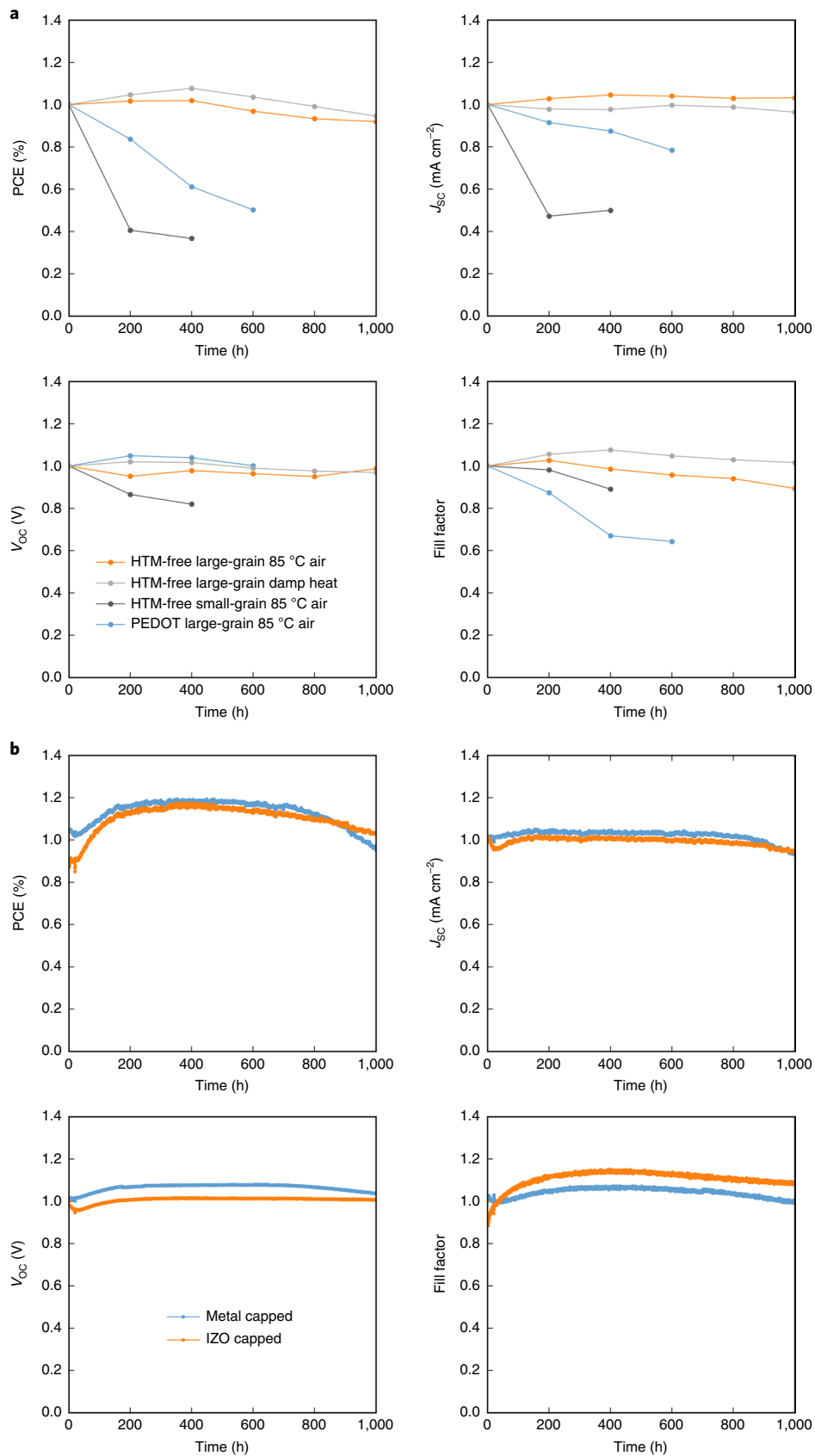


Fig. 4 | Normalized performance as a function of ageing time for $\text{FA}_{0.75}\text{Cs}_{0.25}\text{Sn}_{0.4}\text{Pb}_{0.6}\text{I}_3$ solar cells. a, J - V parameters, measured every 200 h, for devices aged at 85 °C in air (with no encapsulation) or in damp heat (with glass-on-glass encapsulation) (lines are a guide to the eye). b, J - V parameters, measured every 10 min for devices kept at the maximum power point under constant 1sun illumination in nitrogen with no encapsulation. The initial PCE for the metal-capped devices was 15.4% and for IZO-capped devices it was 14.2%.

without encapsulation. The solar cell we designed maintains a better-than-initial performance for over 1,000 h of constant operation under illumination. Future improvements in efficiency are expected from further optimization of the processing of tin–lead perovskites. The results in this article successfully address the main obstacle to tin-containing perovskite solar cells, that of environmental stability, and provide the first demonstration of a 1,000 h operational stability for tin–lead perovskite solar cells. Passing this set of stability tests with a low bandgap tin–lead perovskite solar cell is a crucial step toward commercial viability of tin–lead perovskite single-junction and tandem solar cells.

Methods

Perovskite precursor solution preparation. Perovskite precursor solutions were prepared by dissolving stoichiometric amounts of formamidinium iodide (Greatcell), caesium iodide (Sigma Aldrich), tin(II) iodide (Sigma Aldrich or Alfa Aesar, 99.999% beads) and lead(II) iodide (TCI) in a mixture that comprises *N,N*-dimethylformamide (Sigma Aldrich) and dimethylsulfoxide (DMSO) (Sigma Aldrich) (ratios are detailed below). All perovskite precursor chemicals were used as received and stored inside a nitrogen glove box.

PEDOT:PSS (Clevios P VP AI4083) was diluted 1:2 by volume with methanol just before use and filtered through a PVDF filter with a pore size of 0.2 μm . The PEDOT:PSS solution was stored in a refrigerator in ambient air.

The perovskite solution preparation and film deposition were conducted in a nitrogen glove box typically with 0.1 ppm oxygen and <1 ppm moisture.

Single-junction device fabrication. ITO-coated glass substrates (15 ohm sq^{-1}) were purchased from Thin Film Devices and cleaned by successive sonication in baths of acetone and isopropanol, followed by 10 min of ultraviolet-ozone exposure.

The diluted PEDOT:PSS solution was spin coated at 5,000 r.p.m. for 25 s followed by heating at 150 °C for 10 min, after which the substrates were immediately transferred into a nitrogen glove box for perovskite deposition.

Small-grained $\text{FA}_{0.75}\text{Cs}_{0.25}\text{Sn}_{0.4}\text{Pb}_{0.6}\text{I}_3$. Small-grained films were spin coated using a precursor antisolvent immersion technique described in detail in our previous work¹. A stoichiometric 1.1 M solution of perovskite in 65% dimethylformamide and 35% DMSO was used.

Large-grained $\text{FA}_{0.75}\text{Cs}_{0.25}\text{Sn}_{0.4}\text{Pb}_{0.6}\text{I}_3$. A stoichiometric solution with a higher concentration (1.5 M) and lower DMSO content (15%) was used to prepare the larger-grained films. The film was spun at 5,000 r.p.m. (5,000 r.p.m. s^{-1} acceleration) for 40 s with 200 μl of diethyl ether antisolvent dripped on the spinning film 18 s after the start of spin. The ether drip typically converted the film over several seconds into a clear brown colour. The film was then annealed on a hotplate at 100 °C for 7 min.

Large-grained thick $\text{FA}_{0.75}\text{Cs}_{0.25}\text{Sn}_{0.5}\text{Pb}_{0.5}\text{I}_3$ was used in the side-by-side comparison of bare ITO vs PEDOT devices (Supplementary Fig. 3): a stoichiometric solution of concentration 2.0 M $\text{FA}_{0.75}\text{Cs}_{0.25}\text{Sn}_{0.5}\text{Pb}_{0.5}\text{I}_3$ with 10 mol% SnF_2 in 75% dimethylformamide 25% DMSO was and spin coated on cleaned substrates at 5,000 r.p.m. (5,000 r.p.m. s^{-1} acceleration) for 80 s with 200 μl of diethyl ether antisolvent dripped on the spinning film 25 s after the start of spin. Films were then annealed at 120 °C for 10 min.

After deposition of the perovskite film, 30 nm of C_{60} (Nano-C or Sigma-Aldrich) was deposited by thermal evaporation, typically at a base pressure of 6×10^{-7} torr and a deposition rate of 0.2 \AA s^{-1} for the first 10 nm and 0.5 \AA s^{-1} for the remaining 20 nm.

Metal-capped cells were then finished with a 6 nm layer of BCP (Sigma) and 130 nm of silver (Kurt J. Lesker) both by thermal evaporation. BCP was evaporated at 0.2 \AA s^{-1} . Silver was evaporated at 0.3 \AA s^{-1} for the first 10 nm, and 2 \AA s^{-1} for the remaining 120 nm. The vacuum was broken to change the shadow masks either between the C_{60} and BCP steps or between the BCP and Ag steps; we did not notice any change in device performance between these two cases.

ITO-capped cells were transferred to a different glove box in a sealed jar for the deposition of a 10 nm tin oxide and zinc tin oxide bilayer sputter buffer by pulsed chemical vapour deposition. We used tetrakis-dimethylamino tin(IV) and water as precursors and performed the deposition at 87 °C using a supercycle process similar to that described in our previous work⁴⁰. After this deposition, the cells were transferred, again in a sealed jar, to a sputter chamber loadable from a nitrogen glove box and capped with 200 nm of zinc-doped indium oxide. The IZO was radio frequency sputter deposited from a 2" \times 11" ceramic target (In:Zn = 70:30) at room temperature in an argon–oxygen atmosphere (0.15 vol% O_2 in argon) at a pressure of 5 mtorr using a power of 100 W.

Tandem device fabrication. Monolithic all-perovskite tandem solar cells were fabricated using a procedure described in our recent work⁴. Briefly, the wide-gap cell was fabricated first in a p–i–n configuration on ITO substrates prepared as

above, with poly-TPD (poly(*N,N'*-bis-4-butylphenyl-*N,N'*-bisphenyl)benzidine) spin-coated first as a hole transport layer and then treated with a dynamic spin of PFN-Br (poly((9,9-bis(3'-(*N,N*-dimethylamino)propyl)-2,7-fluorene)-alt-2,7-(9,9-dioctylfluorene))) to improve the perovskite wettability. The wide-gap perovskite, $\text{DMA}_{0.1}\text{FA}_{0.6}\text{Cs}_{0.5}\text{Pb}(\text{I}_{0.8}\text{Br}_{0.2})$ (DMA, dimethylammonium) was then spin coated, followed by thermal evaporation of 1 nm of LiF and 30 nm of C_{60} as an electron transporter. This was followed by a dynamic spin of ethoxylated polyethylenimine for the improved nucleation of a subsequently atomic-layer-deposited layer of 25 nm aluminium-doped zinc oxide, as we recently described⁴. This was followed by radio frequency sputtering of 5 nm of IZO. After this step, the second cell (low-gap tin–lead perovskite cell) was fabricated exactly as described above for single junction solar cells, either with or without a layer of acidic PEDOT:PSS (Clevios P VP AI4083) layer to start.

Solar cell testing. Solar cells were tested on an Oriel Sol3A class AAA solar simulator from Newport inside a nitrogen glove box. The lamp intensity was calibrated using J_{sc} produced in a certified KG2-filtered silicon photodiode. By measuring the external quantum efficiency curve of the solar cell (conducted on a Newport system in ambient air), the spectral mismatch factor was calculated and used to appropriately adjust the intensity of the solar simulator lamp to provide 1 sun illumination. Through this procedure, we verified that the J_{sc} measured corresponded correctly to that the solar cells generated under AM1.5 G solar illumination.

Unless otherwise mentioned, all the scans were taken from 0.9 V to -0.2 V with an interval of 10 mV and a delay of 50 ms between successive steps of measurement. No preconditioning was used before testing.

The total area of all solar cells fabricated was 10.033 mm^2 , as defined by the overlap between the patterned bottom ITO electrode (prepatterned by the ITO substrate supplier, Thin Film Devices) and top metal electrode (patterned using a shadow mask during evaporation or sputter of the top electrode). J – V curves were measured by using a laser-cut metal shadow mask to create an aperture of area 5.8 mm^2 .

Tandem solar cells were tested using a procedure to correctly calibrate the spectral mismatch factor of the solar simulator, as we recently described in detail⁴. Briefly, a 950 nm cutoff filter was used to ensure that both subcells of the tandem experienced the same mismatch factor, which was calculated from the measured lamp spectrum and the measured normalized external quantum efficiency spectra of the individual subcells of the tandem. This ensured that neither subcell of the tandem was artificially over- or underilluminated compared to the correct 1 sun illumination intensity.

XPS. XPS measurements were performed on a Physical Electronics 5600 photoelectron spectrometer, discussed in detail previously⁴¹. Briefly, radiation was produced by a monochromatic 350 W Al $\text{K}\alpha$ excitation centred at 1,486.7 eV. XPS core-level spectra were collected using a step size of 0.1 eV and pass energy of 11.75 eV. The electron binding energy scale was calibrated using the Fermi edge of a gold substrate cleaned by argon ion bombardment. Peak areas were fitted using a Gaussian–Lorentzian peak-fitting algorithm with a Shirley background. Spectra taken with the aluminium source were typically assigned an uncertainty of 0.05 eV. Compositional analyses were typically assigned an uncertainty of 5%. The thin (4 nm) perovskite film used to probe the band positions near the interface with ITO was fabricated by a spin-coating procedure similar to that described above for a large-grained perovskite, but using a perovskite precursor concentration of 10 mM to reduce the film thickness. The film thickness was measured to be 4 nm by atomic force microscopy.

Measurements of d.c. conductance. Perovskite films were spin coated onto clean glass substrates using the procedures described above for large- and small-grained films. Gold electrodes (100 nm thick) were deposited onto the perovskite by thermal evaporation using electrode spacings of 0.75 mm, 1 mm and 3 mm. Conductance was measured by applying a 2 V bias across pairs of electrodes and measuring the current with a Keithley 236 unit. Measurements were conducted inside a nitrogen glove box. All the measurements of current were allowed to stabilize before recording, to ensure the measurement of steady-state electronic conductance rather than any transient effects associated with ion motion in the perovskite. The measurements were conducted in a dark chamber to minimize any effects of photoconductance. Air ageing of the perovskite films for the conductance measurements was done on a hotplate kept at 85 °C in the ambient atmosphere.

Stability testing. For the 85 °C air test, unencapsulated solar cells were placed in a Petri dish in an oven kept at 85 °C in ambient air.

For the damp heat test, glass-on-glass encapsulated solar cells packaged using a procedure similar to that in our recent work¹⁷ were placed in a chamber maintained at 85 °C with 85% relative humidity.

For the operational stability test, solar cells without encapsulation were loaded into a homebuilt degradation testing set-up, dubbed the stability parameter analyser. The set-up consists of a flow chamber to control the environment of the cells, cooling tubes to keep the housing at room temperature, electrical housing and electronics that switch between the devices, measure the J – V curves and hold the

devices under a resistive load, and a light source to provide constant illumination. In this study, the devices were kept in a nitrogen environment underneath a sulfur plasma lamp at ~ 0.8 sun and held under a resistive load of 510 ohms (placing the cells near the maximum power point). Every 30 min, the system removed the resistive load and took a J - V scan using a Keithley 2450 source-measure unit. J - V curves are then analysed to extract the relevant parameters.

SEM. Cross-sectional SEM was conducted on a FEI Magellan 400 XHR scanning electron microscope with a field emission gun source. The images were recorded in an in-lens secondary electron mode using an accelerating voltage of 5 kV at working distances of 1.6–3 mm.

Reporting summary. Further information on research design is available in the Nature Research Reporting Summary linked to this article.

Data availability

The data that support the plots within this article and other findings of this study are available from the corresponding author upon reasonable request.

Received: 11 March 2019; Accepted: 23 August 2019;

Published online: 07 October 2019

References

- Leijtens, T., Bush, K. A., Prasanna, R. & McGehee, M. D. Opportunities and challenges for tandem solar cells using metal halide perovskite semiconductors. *Nat. Energy* **3**, 828–838 (2018).
- Hörantner, M. T. et al. The potential of multijunction perovskite solar cells. *ACS Energy Lett.* **2**, 2506–2513 (2017).
- Eperon, G. E. et al. Perovskite–perovskite tandem photovoltaics with optimized band gaps. *Science* **354**, 861–865 (2016).
- Palmstrom, A. F. et al. Enabling flexible all-perovskite tandem solar cells. *Joule* **3**, 2193–2204 (2019).
- Rajagopal, A., Liang, P.-W., Chueh, C.-C., Yang, Z. & Jen, A. K.-Y. Passivation via graded fullerene heterojunction in low bandgap Pb–Sn binary perovskite photovoltaics. *ACS Energy Lett.* **2**, 2531–2539 (2017).
- Leijtens, T. et al. Tin–lead halide perovskites with improved thermal and air stability for efficient all-perovskite tandem solar cells. *Sustain. Energy Fuels* **2**, 2450–2459 (2018).
- Forgács, D. et al. Efficient monolithic perovskite/perovskite tandem solar cells. *Adv. Energy Mater.* **8**, 1602121 (2016).
- Zhao, D. et al. Efficient two-terminal all-perovskite tandem solar cells enabled by high-quality low-bandgap absorber layers. *Nat. Energy* **3**, 1093–1100 (2018).
- Eperon, G. E., Hörantner, M. T. & Snaith, H. J. Metal halide perovskite tandem and multiple-junction photovoltaics. *Nat. Rev. Chem.* **1**, 0095 (2017).
- Hao, F., Stoumpos, C. C., Chang, R. P. H. & Kanatzidis, M. G. Anomalous band gap behavior in mixed Sn and Pb perovskites enables broadening of absorption spectrum in solar cells. *J. Am. Chem. Soc.* **136**, 8094–8099 (2014).
- Prasanna, R. et al. Band gap tuning via lattice contraction and octahedral tilting in perovskite materials for photovoltaics. *J. Am. Chem. Soc.* **139**, 11117–11124 (2017).
- Noel, N. K. et al. Lead-free organic–inorganic tin halide perovskites for photovoltaic applications. *Energy Environ. Sci.* **7**, 3061–3068 (2014).
- Takahashi, Y. et al. Charge-transport in tin iodide perovskite $\text{CH}_3\text{NH}_3\text{SnI}_3$: origin of high conductivity. *Dalton Trans.* **40**, 5563 (2011).
- Boyd, C. C., Cheacharoen, R., Leijtens, T. & McGehee, M. D. Understanding degradation mechanisms and improving stability of perovskite photovoltaics. *Chem. Rev.* **119**, 3418–3451 (2019).
- Grancini, G. et al. One-year stable perovskite solar cells by 2D/3D interface engineering. *Nat. Commun.* **8**, 15684 (2017).
- Christians, J. A. et al. Tailored interfaces of unencapsulated perovskite solar cells for >1,000 hour operational stability. *Nat. Energy* **3**, 68–74 (2018).
- Cheacharoen, R. et al. Encapsulating perovskite solar cells to withstand damp heat and thermal cycling. *Sustain. Energy Fuels* **2**, 2398–2406 (2018).
- Wang, Z. et al. Efficient and ambient-air-stable solar cells with 2D–3D hetero-structured butylammonium–caesium–formamidinium lead halide perovskites. *Nat. Energy* **2**, 17135– (2017).
- Hou, Y. et al. A generic interface to reduce the efficiency–stability–cost gap of perovskite solar cells. *Science* **358**, 1192–1197 (2017).
- Marshall, K. P., Walker, M., Walton, R. I. & Hattori, R. A. Enhanced stability and efficiency in hole-transport-layer-free CsSnI_3 perovskite photovoltaics. *Nat. Energy* **1**, 1–14 (2016).
- Gao, W. et al. Robust stability of efficient lead-free formamidinium tin iodide perovskite solar cells realized by structural regulation. *J. Phys. Chem. Lett.* **9**, 6999–7006 (2018).
- Leijtens, T., Prasanna, R., Gold-Parker, A., Toney, M. F. & McGehee, M. D. Mechanism of tin oxidation and stabilization by lead substitution in tin halide Perovskites. *ACS Energy Lett.* **2**, 2159–2165 (2017).
- Liao, Y. et al. Highly oriented low-dimensional tin halide perovskites with enhanced stability and photovoltaic performance. *J. Am. Chem. Soc.* **139**, 6693–6699 (2017).
- Liu, C. et al. C_{60} additive-assisted crystallization in $\text{CH}_3\text{NH}_3\text{Pb}_{0.75}\text{Sn}_{0.25}\text{I}_3$ perovskite solar cells with high stability and efficiency. *Nanoscale* **9**, 13967–13975 (2017).
- Chi, D. et al. Composition and interface engineering for efficient and thermally stable Pb–Sn mixed low-bandgap perovskite solar cells. *Adv. Funct. Mater.* **28**, 1804603 (2018).
- Chen, Z. et al. Stable Sn/Pb-based perovskite solar cells with a coherent 2D/3D interface. *iScience* **9**, 337–346 (2018).
- Holzhey, P. & Saliba, M. A full overview of international standards assessing the long-term stability of perovskite solar cells. *J. Mater. Chem. A* **6**, 21794–21808 (2018).
- McMeekin, D. P. et al. A mixed-cation lead mixed-halide perovskite absorber for tandem solar cells. *Science* **351**, 151–155 (2016).
- Turren-Cruz, S. H., Hagfeldt, A. & Saliba, M. Methylammonium-free, high-performance, and stable perovskite solar cells on a planar architecture. *Science* **362**, 449–453 (2018).
- Tan, W., Bowring, A. R., Meng, A. C., McGehee, M. D. & McIntyre, P. C. Thermal stability of mixed cation metal halide perovskites in air. *ACS Appl. Mater. Interfaces* **10**, 5485–5491 (2018).
- Bush, K. A. et al. Thermal and environmental stability of semi-transparent perovskite solar cells for tandems enabled by a solution-processed nanoparticle buffer layer and sputtered ITO electrode. *Adv. Mater.* **28**, 3937–3943 (2016).
- Kraut, E. A., Grant, R. W., Waldrop, J. R. & Kowalczyk, S. P. Precise determination of the valence-band edge in X-ray photoemission spectra: application to measurement of semiconductor interface potentials. *Phys. Rev. Lett.* **44**, 1620–1623 (1980).
- Boyd, C. C. et al. Barrier design to prevent metal-induced degradation and improve thermal stability in perovskite solar cells. *ACS Energy Lett.* **3**, 1772–1778 (2018).
- Zhao, D. et al. Low-bandgap mixed tin–lead iodide perovskite absorbers with long carrier lifetimes for all-perovskite tandem solar cells. *Nat. Energy* **2**, 17018 (2017).
- Xiao, Z. et al. Mixed-halide perovskites with stabilized bandgaps. *Nano Lett.* **17**, 6863–6869 (2017).
- Li, W. et al. Subgrain special boundaries in halide perovskite thin films restrict carrier diffusion. *ACS Energy Lett.* **3**, 2669–2670 (2018).
- Kim, G. Y. et al. Large tunable photoeffect on ion conduction in halide perovskites and implications for photodecomposition. *Nat. Mater.* **17**, 445–449 (2018).
- Milot, R. L. et al. The effects of doping density and temperature on the optoelectronic properties of formamidinium tin triiodide thin films. *Adv. Mater.* **30**, e1804506 (2018).
- Domanski, K. et al. Not all that glitters is gold: metal-migration-induced degradation in perovskite solar cells. *ACS Nano* **10**, 6306–6314 (2016).
- Bush, K. A. et al. 23.6%-efficient monolithic perovskite/silicon tandem solar cells with improved stability. *Nat. Energy* **2**, 17009 (2017).
- Perkins, C. L. & Hasoon, F. S. Surfactant-assisted growth of CdS thin films for photovoltaic applications. *J. Vac. Sci. Technol. A* **24**, 497–504 (2006).

Acknowledgements

This research was supported by the Office of Naval Research award N00014-17-1-2212 and by the US Department of Energy's Office of Energy Efficiency and Renewable Energy (EERE) under Solar Energy Technologies Office (SETO) agreement no. DE-EE0008551. Work at the Stanford Nano Shared Facilities (SNSF) was supported by the National Science Foundation award ECCS-1542152. S.P.D., M.F.A.M.v.H. and G.T. were supported by the US Department of Energy contract no. DE-AC36-08GO28308 with the Alliance for Sustainable Energy LLC, Manager and Operator of the National Renewable Energy Laboratory (NREL). The authors acknowledge support from the De-risking Halide Perovskite Solar Cells and Combined Characterization projects at NREL, funded by the US Department of Energy, Office of Energy Efficiency and Renewable Energy, Solar Energy Technologies Office. J.J.B. was supported by the Office of Naval Research. We thank S. U. Nanayakkara for performing the atomic force microscopy measurements.

Author contributions

R.P. and T.L., under the supervision of M.D.M., designed the study. R.P. and T.L. designed the experiments, fabricated solar cells and conducted and interpreted various characterization. S.P.D. and G.T. conducted and interpreted all the XPS measurements. S.P.D., E.J.W., T.L., R.P., J.A.R., G.E.E., S.A.S., J.W., M.F.A.M.v.H., A.E.P. and C.C.B. fabricated devices and/or conducted various stability tests. C.d.P. performed the SEM characterization. R.P. wrote the first draft of the paper. M.D.M., J.J.B. and S.F.B. supervised the work. All the authors contributed to the analysis of the results and revision of the paper.

Competing interests

T.L. and G.E.E. are co-founders of, and M.D.M. is an advisor to, Swift Solar Inc., a company commercializing perovskite solar cells. All other authors declare no competing interests.

Additional information

Supplementary information is available for this paper at <https://doi.org/10.1038/s41560-019-0471-6>.

Correspondence and requests for materials should be addressed to M.D.M.

Reprints and permissions information is available at www.nature.com/reprints.

Publisher's note Springer Nature remains neutral with regard to jurisdictional claims in published maps and institutional affiliations.

© The Author(s), under exclusive licence to Springer Nature Limited 2019